

## Ultrafine jagged platinum nanowires enable high platinum mass activity for the oxygen reduction reaction

Mufan Li<sup>1</sup>, Zipeng Zhao<sup>2</sup>, Tao Cheng<sup>3</sup>, Alessandro Fortunelli<sup>3,4</sup>, Chih-Yen Chen<sup>2</sup>, Rong Yu<sup>5</sup>, Qinghua Zhang<sup>6</sup>, Lin Gu<sup>6</sup>, Boris Merinov<sup>3</sup>, Zhaoyang Lin<sup>1</sup>, Enbo Zhu<sup>2</sup>, Qinghua Zhang<sup>6</sup>, Ted Yu<sup>3,7</sup>, Qingying Jia<sup>8</sup>, Jinghua Guo<sup>9</sup>, Liang Zhang<sup>9</sup>, William A. Goddard III<sup>3\*</sup>, Yu Huang<sup>2,10\*</sup> and Xiangfeng Duan<sup>1,10\*</sup>

<sup>1</sup>Department of Chemistry and Biochemistry, University of California, Los Angeles, California 90095, United States

<sup>2</sup>Department of Materials Science and Engineering, University of California, Los Angeles, California 90095, United States

<sup>3</sup>Materials and Process Simulation Center, California Institute of Technology, Pasadena, California 91125, United States

<sup>4</sup>CNR-ICCOM, Consiglio Nazionale delle Ricerche, 56124, Pisa, Italy

<sup>5</sup>National Center for Electron Microscopy in Beijing, School of Materials Science and Engineering, Tsinghua University, Beijing 100084, P. R. China

<sup>6</sup>Institute of Physics, Chinese Academy of Sciences, Beijing 100190, P. R. China

<sup>7</sup>Department of Chemical Engineering, California State University, Long Beach, California 90840, United States

<sup>8</sup>Department of Chemistry and Chemical Biology, Northeastern University, Boston, Massachusetts 02115, United States

<sup>9</sup>Materials Sciences Division, Lawrence Berkeley National Laboratory, Berkeley, California 94720, United States

<sup>10</sup>California NanoSystems Institute, University of California, Los Angeles, California 90095, United States

\*Correspondence author. Email: wag@wag.caltech.edu (W.G.); yhuang@seas.ucla.edu (Y.H.); xduan@chem.ucla.edu (X.D.)

**Abstract:** Improving the platinum (Pt) mass activity for the oxygen reduction reaction (ORR) should optimize both the specific activity and the electrochemical active surface area (ECSA). We show that solution-synthesized Pt/NiO core/shell nanowires can be readily converted into PtNi alloy nanowires through a post-synthesis thermal annealing process, and then transformed into jagged Pt nanowires via an electrochemical dealloying process. The jagged nanowires exhibit an ECSA of 118 square meters per gram Pt and a specific activity of 11.5 milliamperes per square centimeter for ORR (at 0.9 volt versus the reversible hydrogen electrode) for a mass activity of 13.6 ampere per milligram Pt, or nearly doubles previously reported best values. Reactive molecular dynamics simulations suggest that highly stressed, undercoordinated rhombohedral-rich surface configurations of the jagged nanowires enhanced ORR activity versus more relaxed surfaces.

**One Sentence Summary:** We report the preparation of ultra-fine jagged Pt nanowires with highly stressed, under-coordinated rhombi-rich surface configurations that deliver a record high

mass activity for the oxygen reduction reaction, a breakthrough that addresses the critical limiting factor in hydrogen fuel cells and might make automotive fuel cells economical enough to enable a dramatic decrease in auto related CO<sub>2</sub> generation.

Platinum (Pt) represents the essential element for catalyzing the oxygen reduction reaction (ORR) (1-3). However, the catalyzed ORR rate remains sluggish that the high cost of Pt becomes the primary limiting factor preventing the widespread adoption of fuel cells (4, 5), and higher Pt mass activity (the catalytic activity per given mass of Pt) must be achieved. The Pt mass activity is determined by the specific activity (SA, normalized by surface area) and the electrochemically active surface area (ECSA, normalized by mass). The SA can be optimized by tuning the chemical environment, including chemical composition (6-9), exposed catalytic surface (1, 10-12), and Pt coordination environment (13-16). To date, the highest SAs has generally been achieved on single crystal surfaces or well-defined nanoparticles (NPs) with specifically engineered facet structure and alloy compositions. For example, the Pt<sub>3</sub>Ni (111) single crystal facet (1) and subsequently Pt<sub>3</sub>Ni octahedral NPs have been shown to exhibit ORR-favorable surface structure for greatly enhanced activity (17-19), but such alloys typically suffer from insufficient stability because of electrochemical leaching of Ni during electrochemical cycling and decreased ECSA because of agglomeration of the NPs. Introduction of Mo surface dopants can mitigate such leaching processes and help maintain the ORR-favorable Pt<sub>3</sub>Ni (111) surface for enhanced activity and stability (19). Although high SA has been achieved on these structures, the reported ECSA for these optimized structures are typically limited to ~ 70 m<sup>2</sup>/g<sub>Pt</sub>. On the other hand, the ECSA may be improved by tailoring the geometrical factors including creating ultrafine nanostructures (20, 21) or core/shell nanostructures with an ultrathin Pt skin (22-24) that exposes most Pt atoms on the surface.

To boost both Pt mass activity and Pt utilization efficiency, an ideal catalyst should have an ORR-favorable chemical environment for high SA, optimized geometric factors for high ECSA (20-24), and a mechanism to maintain these high values for long periods of operation. We report the preparation of ultrafine jagged Pt nanowires (J-PtNWs) (diameter ~2.2 nm) with rich ORR-favorable rhombic configurations to lead to an SA of 11.5 mA/cm<sup>2</sup> (at 0.9 V vs. RHE: reversible hydrogen electrode) and an ECSA of 118 m<sup>2</sup>/g<sub>Pt</sub>. Together, these J-PtNWs deliver mass activity of 13.6 A/mg<sub>Pt</sub> (at 0.9 V vs. RHE), which is ~50 times higher than state-of-the-art commercial Pt/C catalyst, and nearly doubles the highest previously reported mass activity values of 6.98 A/mg<sub>Pt</sub> (19) and 5.7 A/mg<sub>Pt</sub> (23). Finally, the PtNi alloy NWs were electrochemically dealloyed to produce ultrafine pure Pt NWs with jagged surfaces. Here, Ni does not play an active electronic or structural role but is sacrificial, as it is leached entirely to form pure J-PtNWs.

We prepared Pt/NiO core/shell NWs by reducing platinum (II) acetylacetonate [Pt(acac)<sub>2</sub>] and nickel(II) acetylacetonate [Ni(acac)<sub>2</sub>] in a mixture solvent of 1-octadecene (ODE) and oleylamine (OAm) (25). Transmission electron microscopy (TEM) studies show that the as-synthesized NWs exhibit an apparent core/shell structure with a contrast of darker core and lighter shell. The NWs have a typical overall diameter ~ 5 nm or less, and a length between about 250 to 300 nm (Fig. 1A, Fig. S1A). High-resolution TEM (HRTEM) studies confirm the core/shell structure with a typical core diameter of 2.0 nm ± 0.2 nm (Fig. 1D). The shell shows well-resolved lattice fringes with the spacing of 0.24 nm, corresponding to the (111) lattice planes of face-centered cubic (fcc) NiO (Fig. 1D), and the core displays a primary lattice spacing of 0.23 nm, corresponding to Pt (111) planes (Fig. 1D).

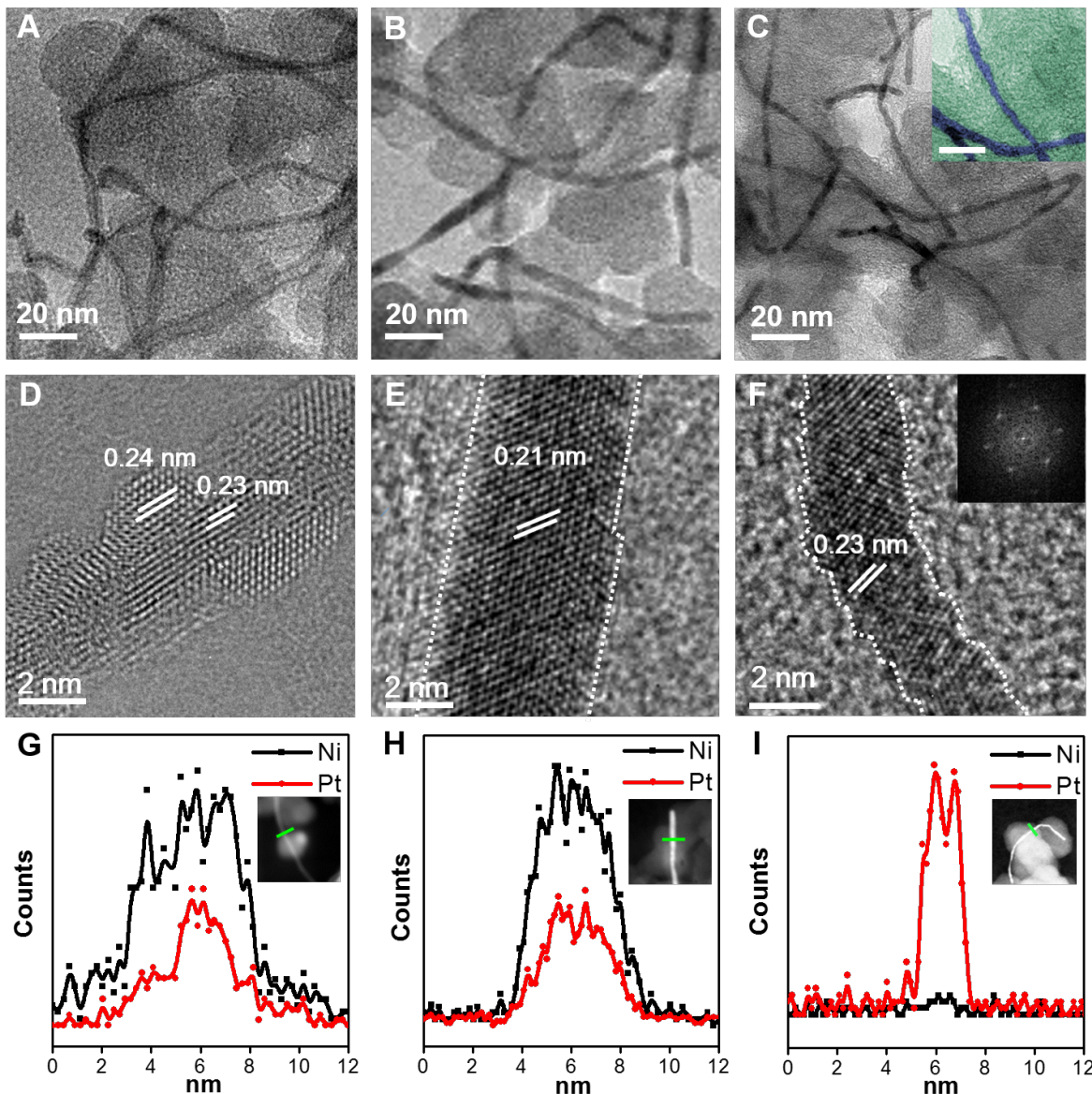


**Fig. 1. Structure and composition characterization of different stages of the J-PtNW evolution process.** (A, B and C) Representative TEM images and (D, E and F) HRTEM images of the Pt/NiO core/shell NWs, the PtNi alloy NWs and the J-PtNWs supported on carbon, respectively. The inset in C shows a false-colored, zoomed-in image of the J-PtNWs, highlighting the rough surface (scale bar: 10 nm). The inset in F shows the corresponding fast Fourier transform (FFT) image. The dashed lines in E and F show the outline of the NWs, highlighting the rough surface of the J-PtNWs. (G, H and I) EDS line-scan profiles of the corresponding NWs show clearly the evolution from the Pt/NiO core/shell, to PtNi alloy, and then pure Pt NWs.

These Pt/NiO NWs were then loaded onto carbon black and annealed in an argon/hydrogen mixture (Ar/H<sub>2</sub>: 97/3) at 450 °C to produce PtNi alloy NWs. The overall morphology of the NW was maintained without obvious change in length or diameter, but the apparent core/shell contrast disappeared (Fig. 1B), suggesting the formation of uniform PtNi alloy NWs. The

HRTEM image of the annealed NW confirms a uniform contrast with a well-resolved lattice spacing of 0.21 nm throughout the entire NW diameter (Fig. 1E), consistent with the (111) lattice spacing of the PtNi alloy. This evolution from the initial core/shell NWs before annealing to uniform alloy NWs after annealing was also confirmed by high-angle annular dark-field scanning transmission electron microscope (HAADF-STEM) studies (Fig. S1C, D).

Our energy-dispersive x-ray spectroscopy (EDS) elemental analysis shows that the overall Pt/Ni ratio remains essentially the same (Pt/Ni: 15/85) before and after annealing (Fig. S3A, B). The EDS line scan profile of the as-prepared NWs also confirms the core/shell structure with a Pt core (Fig. 1G) that diffuses homogeneously throughout the entire NW after annealing (Fig. 1H). X-ray diffraction (XRD) studies also confirm the evolution of the initial Pt/NiO core/shell configurations into a fully alloyed PtNi NW structure (Fig. S4). Furthermore, x-ray photoelectron spectroscopy (XPS) studies further demonstrate that the nickel valence state changed from  $\text{Ni}^{x+}$  in the Pt/NiO core/shell NWs to mostly  $\text{Ni}^0$  after annealing, consistent with the formation PtNi alloy (Fig. S5).

We believe that the NW geometry is essential for ensuring the thermal stability of these ultrafine NWs under high temperature annealing. For example, a similar thermal annealing process applied to ultrafine PtNi NPs led to substantial aggregation of the NPs (a size increase from  $\sim 7$  nm before to 10 to 30 nm) (Fig. S2), which could be partly attributed to the movement and fusion of NPs. In contrast, NWs supported on carbon black have multiple anchoring points and their mobility is much lower compared to NPs with single point contact on carbon support.

An electrochemical de-alloying (leaching) process was used to gradually remove Ni atoms from the PtNi alloy NWs, which allowed the rearrangement of Pt atoms on surface to form the J-PtNWs. We performed cyclic voltammetry (CV) in  $\text{N}_2$ -saturated 0.1 M  $\text{HClO}_4$  solution (0.05 V to 1.1 V vs. RHE) with a sweep rate of  $100 \text{ mVs}^{-1}$  (Fig. 2A). Based on the CV sweeps, the  $\text{ECSA}_{\text{Hupd}}$  was derived from the  $\text{H}_{\text{upd}}$  adsorption/desorption peak areas ( $0.05 \text{ V} < E < 0.35 \text{ V}$ ) and the total mass of the loaded Pt. The PtNi alloy NWs initially showed an essentially negligible  $\text{ECSA}_{\text{Hupd}}$  during the first CV cycle. The  $\text{ECSA}_{\text{Hupd}}$  increased steadily with the increasing number of CV cycles (Fig. 2B). Importantly, the NWs were fully activated in  $\sim 160$  CV cycles to reach a stable  $\text{ECSA}_{\text{Hupd}}$  up to  $118 \text{ cm}^2/\text{mg}_{\text{Pt}}$ , versus previous highest reported values of  $\sim 70 \text{ cm}^2/\text{mg}_{\text{Pt}}$  (Table 1).

Structural and elemental studies were performed to characterize the fully activated NWs after CV cycles. Low-resolution TEM images show that the overall NW structure was well-maintained after the electrochemical de-alloying process (Fig. 1C). The HRTEM images show that the overall diameter of the NW shrank from  $\sim 5.0$  to  $\sim 2.2$  nm after the CV cycles, with well-resolved lattice spacing of 0.23 nm, again consistent with Pt (111) (Fig. 1F). The EDS line scan showed that Pt was the only dominant element in the resulting NWs (Fig. 1I), further confirming complete Ni leaching. In addition, the CV scan of the fully activated NWs (after 160 CV cycles) in 0.1 M KOH showed an absence of typical  $\text{Ni}^{2+}/\text{Ni}^{3+}$  redox signatures, in contrast to the partially activated (150 cycles) PtNi alloy NWs in which the  $\text{Ni}^{2+}/\text{Ni}^{3+}$  redox peaks were prominent (Fig. S6). We also conducted CO-stripping experiment to determine the  $\text{ECSA}_{\text{CO}}$  of J-PtNWs (Fig. S7). The resulting ratio of  $\text{ECSA}_{\text{Hupd}} : \text{ECSA}_{\text{CO}}$  is 1.00:1.05, which is in agreement with that of typical pure Pt material (22). Furthermore, TEM studies of the de-alloyed NWs also showed a highly jagged surface (Fig. 1 C, inset in C and F) with rich atomic steps, in contrast to relatively smooth surface observed in typical synthetic PtNWs (Fig. S1B). Based on these observations, we denote the resulting nanowires as the jagged PtNWs (J-PtNWs).

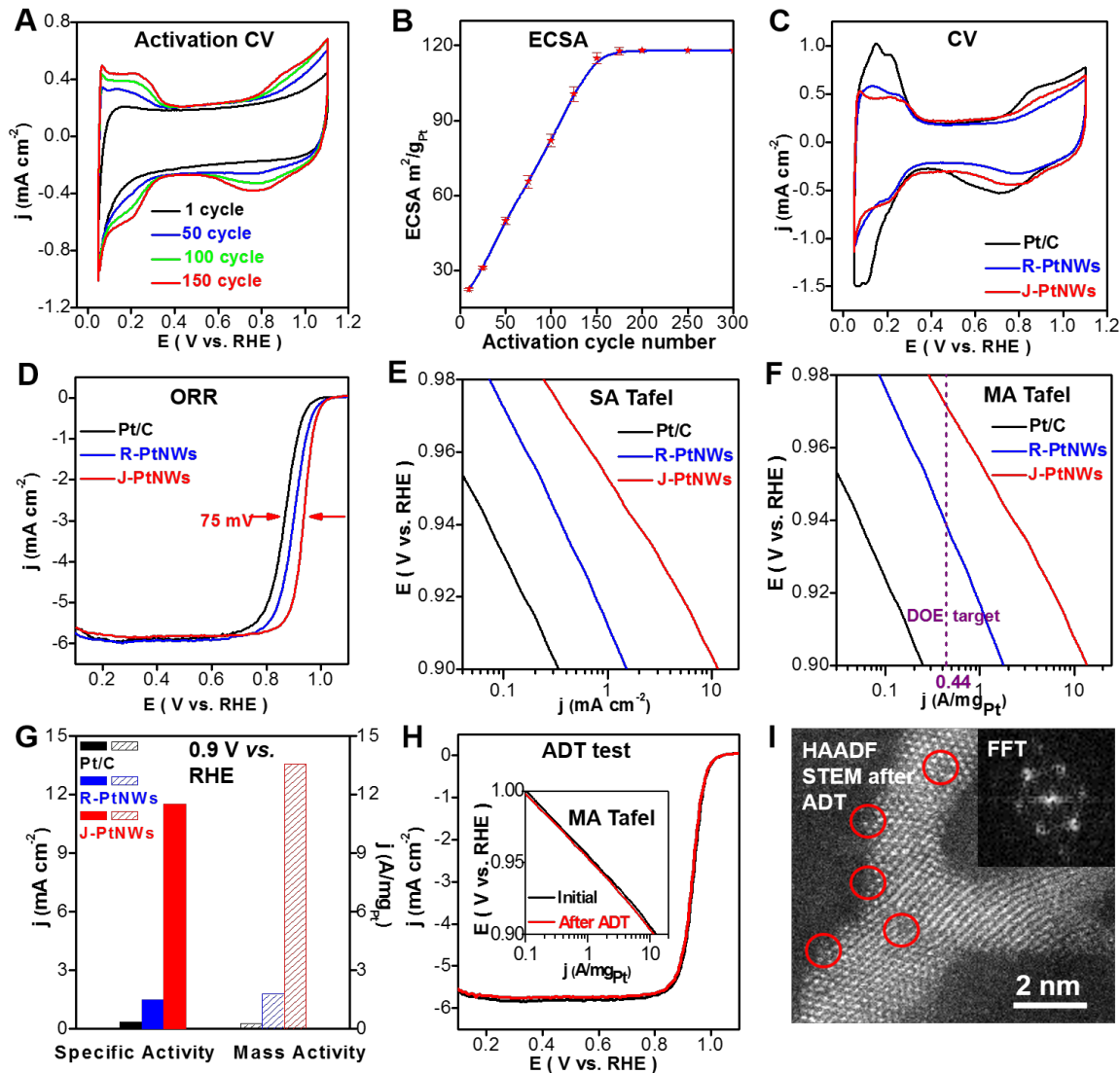


**Fig. 2. Electrochemical performance of the jagged PtNWs (J-PtNWs) vs. regular synthetic PtNWs (R-PtNWs) and commercial Pt/C.** (A) Cyclic voltammetry (CV) curves corresponding to different activation cycles of the de-alloying process, clearly indicating the increasing surface area with the increasing number of CV cycles. (B) The evolution of ECSA with the increasing CV cycles, showing that 150 cycles are sufficient to construct the J-PtNW and reach a stable ECSA. (C and D) CV and ORR polarization curves for the J-PtNWs, the R-PtNWs, and the Pt/C, respectively. (E and F) Specific activity (SA) and mass activity (MA) Tafel plot for the J-PtNWs, the R-PtNWs, and the Pt/C, respectively. The purple dash line indicates the 2017 mass activity target (@ 0.90V vs. RHE) set by US Department of Energy (DOE). (G) The comparison of specific activities and mass activities of the J-PtNWs, the R-PtNWs, and the Pt/C at 0.9 V vs. RHE, showing that the J-PtNWs deliver 33 times higher specific activity or 52 times higher mass activity than Pt/C. (H) ORR polarization curves and mass activity Tafel plot (inset) for the J-PtNWs before and after 6000 CV cycles between 0.6 and 1.0 V versus RHE, showing little loss in activity. The scan rate for the Accelerated Durability Test (ADT) is 100 mVs<sup>-1</sup>. (I) High-resolution HAADF-STEM image of the J-PtNWs after ADT test. The circled areas indicate defective regions with missing atoms. The inset shows the corresponding FFT image.

The electrocatalytic performance of the resulting NWs was compared with commercial Pt/C catalyst (10 % mass loading of ~ 3 to 5 nm Pt NPs on carbon support) and directly synthesized regular PtNWs (R-PtNWs, ~ 1.8 nm diameter, Fig. S1B) with relatively smooth surface (25). To assess the ORR activity, all catalysts were loaded onto glassy carbon electrodes (Pt mass loading: 2.2  $\mu\text{g}/\text{cm}^2$  for J-PtNWs, 2.55  $\mu\text{g}/\text{cm}^2$  for R-PtNWs and 7.65  $\mu\text{g}/\text{cm}^2$  for Pt/C catalyst). We used CV to measure the ECSA (Fig. 2C). Overall, the J-PtNWs, R-PtNWs and Pt/C catalysts showed an ECSA of 118, 110, and 74  $\text{m}^2/\text{g}_{\text{Pt}}$ , respectively (Table 1). The synthetic R-PtNWs also exhibited a rather high ECSA that may be related to their ultrasmall diameters (~ 1.8 nm).

Fig. 2D shows the ORR polarization curves normalized by glassy carbon electrode geometric area (0.196  $\text{cm}^2$ ). The half-wave potential for the J-PtNWs was at 0.935 V, which is considerably higher than those of the commercial Pt/C (0.86 V) and the R-PtNWs (0.90 V), suggesting excellent ORR activity of the J-PtNWs. The Koutecky-Levich equation was used to calculate the kinetic current by considering the mass-transport correction. The specific and mass activities were normalized by the ECSA or the total mass of the loaded Pt, respectively. Overall, the J-PtNWs showed a specific activity of 11.5  $\text{mA}/\text{cm}^2$  at 0.90 V vs. RHE, far higher than 0.35  $\text{mA}/\text{cm}^2$  for the Pt/C or 1.70  $\text{mA}/\text{cm}^2$  for the R-PtNWs tested under the same conditions. Together with their ultrahigh specific surface area, the J-PtNWs deliver a high mass activity of 13.6  $\text{A}/\text{mg}_{\text{Pt}}$  at 0.9 V vs. RHE, which is 52 times higher than that of the 10 % wt Pt/C (0.26  $\text{A}/\text{mg}_{\text{Pt}}$ ), and more than 7 times higher than that of the R-PtNWs (1.76  $\text{A}/\text{mg}_{\text{Pt}}$ ) (Fig. 2G) (Table 1). The mass activity achieved in the J-PtNWs nearly doubles the highest previously reported mass activity value of 6.98  $\text{A}/\text{mg}_{\text{Pt}}$  (19) and 5.7  $\text{A}/\text{mg}_{\text{Pt}}$  (23). Importantly, the observed mass activity was highly reproducible and was between 10.8 and 13.8  $\text{A}/\text{mg}_{\text{Pt}}$  in >15 independently tested J-PtNW electrodes.

Because the current value at 0.90 V is already near the diffusion-limited current in ORR polarization curve, we also compared mass activity at half-wave potential of the J-PtNWs (0.935 V) in Table 1. Our analysis shows that the J-PtNWs still exhibit an impressive 48 times higher mass activity than that of Pt/C. The specific activity Tafel plots (Fig. 2E) exhibit a slope of 51, 72 and 74  $\text{mV dec}^{-1}$  for J-PtNWs, R-PtNWs and Pt/C, respectively. A considerably smaller slope achieved in the J-PtNWs suggests significantly improved kinetics for ORR. Remarkably, the mass activity Tafel plot (Fig. 2F) shows that the J-PtNWs deliver 30 times higher mass activity than the 2017 target set by US Department of Energy (0.44  $\text{A}/\text{mg}_{\text{Pt}}$  at 0.90 V for MEA, highlighted by purple dash line in Fig. 2F). The J-PtNW can deliver the DOE targeted mass activity at 0.975 V (RHE), thus significantly reducing the over-potential by 0.075 V.

The J-PtNWs exhibit higher specific activity and mass activity (11.5  $\text{mA}/\text{cm}^2$  or 13.6  $\text{A}/\text{mg}_{\text{Pt}}$  at 0.9 V) than those of R-PtNWs (1.70  $\text{mA}/\text{cm}^2$  or 1.87  $\text{A}/\text{mg}_{\text{Pt}}$  at 0.9 V), despite similar ECSA values (118  $\text{m}^2/\text{g}_{\text{Pt}}$  for 2.2 nm J-PtNWs and 110  $\text{m}^2/\text{g}_{\text{Pt}}$  for 1.8 nm R-PtNWs). Compared with Pt/C, the J-PtNWs show a 33 times increase in specific activity at 0.90 V vs. RHE, which suggests that the activation energy for the rate-determining step of ORR on the J-PtNWs is reduced by 0.090 eV from that of Pt/C [ $\Delta E_{act} = k_B T \ln(SA_{\text{J-PtNW}}/SA_{\text{Pt/C}})$ ], where  $\Delta E_{act}$  is difference in activation energy,  $k_B$  Boltzmann's constant,  $T$  temperature,  $SA_{\text{J-PtNW}}$  specific activity of J-PtNWs,  $SA_{\text{Pt/C}}$  specific activity of Pt/C]. This decrease is plausible decrease based on our various ORR computations (16).

**Table 1. Electrochemically active surface area, specific activity, half-wave potential and mass activity of J-PtNWs/C, R-PtNWs/C, Pt/C catalysts, in comparison with those in several representative recent studies.**

	ECSA (m <sup>2</sup> /g <sub>Pt</sub> )	SA (mA/cm <sup>2</sup> ) @ 0.90 V	Half-wave potential (V)	Mass activity (A/mg <sub>Pt</sub> )	
				@ 0.90 V	@ 0.935 V
<b>J-PtNWs/C (this work)</b>	118	11.5	0.935	13.6	2.87
<b>R-PtNWs/C (this work)</b>	110	1.59	0.899	1.76	0.5
<b>Pt/C (this work)</b>	74	0.35	0.860	0.26	0.06
<b>Octahedron Pt<sub>2.5</sub>Ni/C</b> ( <i>ref.17</i> )	21	NA	NA	3.3	NA
<b>Nanoframe Pt<sub>3</sub>Ni/C</b> ( <i>ref.23</i> )	67.2	NA	NA	5.7	NA
<b>Mo-Pt<sub>3</sub>Ni/C</b> ( <i>ref.19</i> )	67.7	10.3	NA	6.98	NA
<b>DOE 2017 target</b>	NA	NA	NA	0.44	NA

We evaluated the durability of the J-PtNWs using accelerated deterioration tests (ADT) under a sweep rate of 100 mVs<sup>-1</sup> between 0.6 V and 1.0 V in O<sub>2</sub>-saturated 0.1 M HClO<sub>4</sub>. After 6000 cycles, the ECSA dropped only by ~7 %, and the specific activity dropped by only ~5.5 %, and together the mass activity dropped by only 12 % (Fig. 2H). The retention of high ECSA in J-PtNWs during ADT is in stark contrast to that of Pt/C, which showed a much larger loss (~30%) in ECSA during similar ADT tests. Ultrafine nanostructures (*e.g.*, ~ 2 nm) have shown severely worse stability compared to their bulk counterpart (26, 27). The unique 1D geometry of nanowires and the multipoint contacts with carbon support might also deter the Ostwald ripening process usually observed in spherical NPs (Fig. S8), contributing to the excellent durability. Indeed, our TEM studies before and after ADT test showed little change in the overall morphology or size of the J-PtNWs on carbon support (Fig. S9). High-resolution STEM studies showed that the jagged surface (with defective sites) was largely preserved after 6000 cycles (Fig. 2I).

To gain further insight on how the J-PtNWs could deliver dramatically higher ORR activity, we conducted reactive molecular dynamics (RMD) studies using the reactive force field (ReaxFF) (28) to simulate the formation of J-PtNWs by leaching Ni atoms from an initial Pt<sub>15</sub>Ni<sub>85</sub> alloy NWs (16), and a second-moment-approximation (SMA) tight-binding potential (29) for final local optimization and prediction of Pt-Pt distances. (25). The RMD simulation resulted in a pure Pt NW containing 7,165 Pt atoms (in a length of ~ 46 nm) with a diameter of ~ 2.2 nm and highly jagged surface (Fig. 3A). Notably, the overall morphology of the predicted J-PtNWs resembles closely the experimentally obtained J-PtNWs as shown in TEM images in Fig. 1, both of which show modulating thread-like segments about 2.2 nm in diameter, containing striction regions, bending points and jagged surfaces.

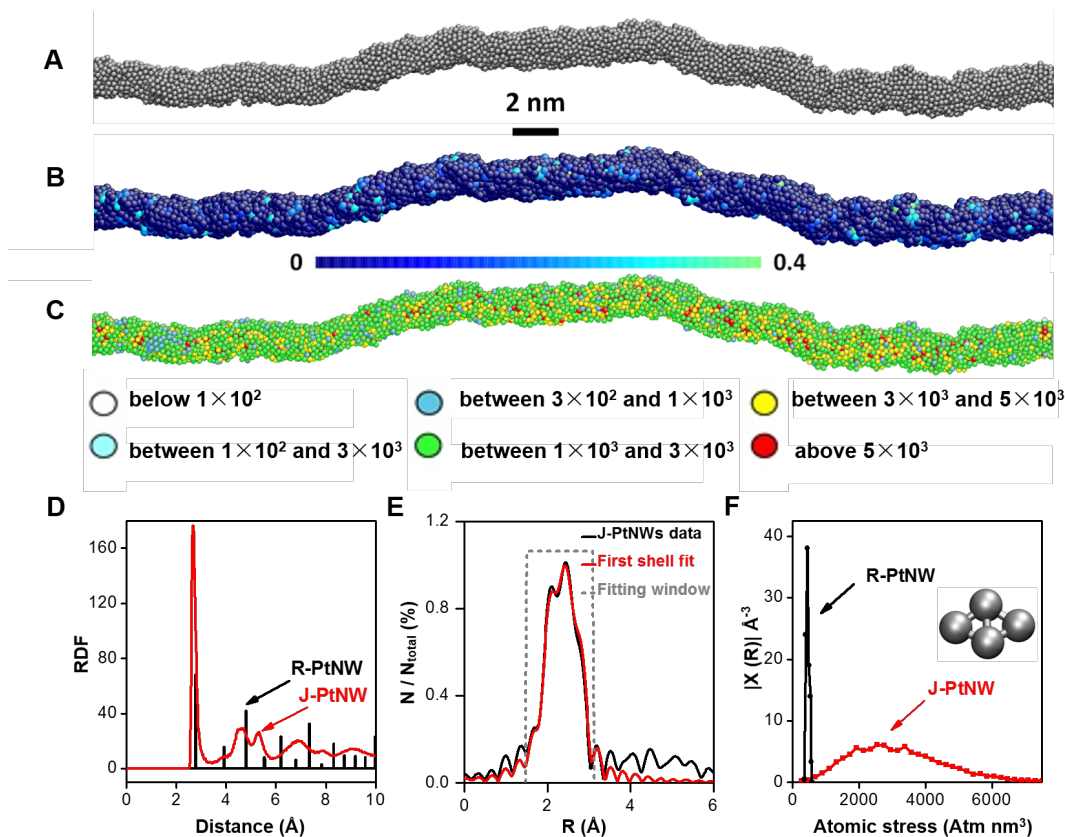


**Fig. 3. Structural analysis of the J-PtNWs obtained from Re axFF reactive molecular dynamics and x-ray absorption spectroscopy.** (A) Pictorial illustrations of the final structure of a Pt J-NW generated by Reactive Molecular Dynamics simulations, with an average diameter of  $\sim 2.2$  nm and length of  $\sim 46$  nm. (B) J-PtNW with colored atoms to show the 5-fold index. (C) J-PtNW with colored atoms to show distribution of atomic stress (in  $\text{atm}\cdot\text{nm}^3$ ). (D) Pt-Pt radial distribution function (RDF) of the SMA-predicted J-PtNW (red) compared with the peaks of the RDF for the regular PtNW (black). (E) Pt  $L_3$  edge FT-EXAFS spectrum (black) collected ex situ and the corresponding first shell least-squares fit (red) for the J-PtNWs. (F) Distribution of the absolute values of the average atomic stress on surface rhombi for the R-PtNWs (black) and the J-PtNWs (red). A rhombus is an ensemble of 4 atoms arranged as two equilateral triangles sharing one edge as shown in the inset.

The predicted radial distribution function (RDF) for the J-PtNW exhibits a well-defined first-neighbor peak at about  $2.70 \text{ \AA}$  (Fig. 3D), which is  $\sim 2.2$  to  $2.5\%$  shorter than the Pt-Pt first-neighbor distance predicted for the R-PtNWs ( $2.76 \text{ \AA}$ ) and the bulk Pt crystal ( $2.77 \text{ \AA}$ ), whereas the peaks associated with the second and further neighbors are much broader and more blurred, similar to those reported in nanoporous NPs (16). These predicted Pt-Pt first-neighbor distance are well confirmed by the EXAFS analysis (Fig. 3E, Fig. S10, Table S1), which reveals that the first shell Pt-Pt bond length in the J-PtNWs ( $2.71 \text{ \AA}$ ) is  $\sim 1.8\%$  shorter than that of the Pt foil ( $2.76 \text{ \AA}$ ).

Nanowires with small diameters ( $\sim 2.2$  nm in this case) inherently have ultrahigh surface area that can be further enhanced by the surface roughness of a jagged morphology. We calculated the van der Waals (vdW) surface area of the simulated J-PtNWs to be  $\sim 110 \text{ m}^2/\text{g}_{\text{Pt}}$  (Table S2),

which agrees well with our experimental value derived from the ECSA ( $118 \text{ m}^2/\text{g}_{\text{Pt}}$ ). However, the enhancement of surface area alone cannot fully account for the observed ORR mass activity. Stressed and under coordinated crystalline-like surface rhombi can dramatically decrease the reaction barrier of the rate determining steps of ORR, thus, improving specific ORR activity (16). Surface rhombi are an ensemble of 4 atoms arranged as two equilateral triangles sharing one edge (see the inset in Fig. 4F) and resembling the triangular tessellation of an fcc (111) surface, which we find to be superior to a square tessellation for ORR activity in the same way that the fcc (111) surface is more ORR-active than other compact *fcc* surfaces such as fcc (100) (1, 30). Moreover, rhombi that are stressed and under coordinated but still crystalline-like exhibit smaller overall energy barriers for ORR than those encountered on the rhombi of the fcc (111) surface, as predicted via density-functional theory (DFT) calculations (16).

Several factors could contribute to the greatly enhanced ORR activity in the J-PtNWs. First, our analysis shows that the coordination number of surface atoms in the J-PtNWs ranges mostly between 6 and 8 (Fig. S11A), indicating that these surface atoms are under-coordinated when compared to typical crystal surfaces (with coordination numbers of 8 or 9 for (100) or (111) facets, respectively). Despite the low-coordination number and jagged feature, the crystalline-like character of surface atoms in J-PtNWs is confirmed from common neighbor analysis (CNA) (31-33). CNA result shows that the ratio of CNA [5, 5, 5] triplets (a finger print of icosahedral structure) (29, 34) to the total number of CNA triplets is rather low (84% of the atoms have a ratio below 0.0065) (Fig. 3B). Because the bonded pairs of type [5, 5, 5] are characteristic of icosahedral order, this low [5, 5, 5] ratio indicates a more crystalline-like feature (32) for our established model, which is also a crucial factor for enhancing ORR activity (16). Indeed, such crystalline-like character of simulation model is consistent with the experimental FFT images (insets in Fig. 1F and 2I) showing that the J-PtNWs remain fcc-like after CV activation and repeated cycling test. Additionally, the distribution of rhombus dihedral angles (Fig. S11B) shows that most of the dihedral angles formed between the two triangles of the rhombus range between  $156^\circ$  and  $180^\circ$ . Comparing with  $180^\circ$  for typical crystalline Pt (111) facet, this statistical analysis further confirms the high-crystallinity nature of the J-PtNWs, which is favorable for increased reactivity (16). Second, the surface atoms in the J-PtNWs exhibit rather high value of Cauchy atomic stress times atomic volume about 10 times larger than that for regular (100) or (111) facets (Fig. 3, C and F), as also confirmed by simulated and EXAFS derived Pt-Pt distances (Fig. 3, D and E). To provide further information on surface energetics, we report that the ReaxFF surface energy of the J-PtNW is  $2.7 \text{ J/m}^2$  that is higher than the value for the Pt(111) surface of  $1.7 \text{ J/m}^2$  (this latter ReaxFF value is in very good agreement with quantum mechanics and experimental values). This mechanical strain can decrease the binding energy of adsorbents on close-packed surfaces, which can make the surfaces more active (32, 35-36), further contributing to the activity enhancement. Finally and importantly, we found that the J-PtNWs possess both a large ECSA (see Table S2 of the Supplementary Material) and exhibit an unusually high number of the ORR-favorable rhombic structures on the surface. There are 76% rhombi per surface atom in the J-PtNW surface (Table S2), considerably higher than 57% previously reported for the nanoporous Pt-NPs (16).

We also prepared similar J-PtNWs by electrochemical dealloying PtCo NWs and achieved an ORR activity of  $8.1 \text{ A/mg}_{\text{Pt}}$  (Fig. S12, S13), that was higher than the highest number reported previously ( $6.98 \text{ A/mg}_{\text{Pt}}$ ). We attribute the lower mass activity compared to PtNi derived J-PtNWs to the slightly larger diameter of the resulting NWs ( $\sim 2.5$  vs.  $\sim 2.2$  nm) leading to a smaller ECSA ( $92 \text{ m}^2/\text{g}_{\text{Pt}}$  vs.  $118 \text{ m}^2/\text{g}_{\text{Pt}}$ ) and possibly to differences in dealloying mechanism of Co with respect

to Ni. These studies further demonstrate the validity and generality of our approach to derive highly ORR active J-PtNWs from alloy NWs.

#### REFERENCES AND NOTES:

1. V. R. Stamenkovic, B. Fowler, B. S. Mun, G. Wang, P. N. Ross, C. A. Lucas, N. M. Marković, Improved oxygen reduction activity on Pt<sub>3</sub>Ni(111) *via* increased surface site availability. *Science* **315**, 493–497 (2007).
2. N. S. Porter, H. Wu, Z. Quan, J. Fang, Shape-control and electrocatalytic activity-enhancement of Pt-based bimetallic nanocrystals. *Acc. Chem. Res.* **46**, 1867–1877 (2013).
3. J. Wu, H. Yang, Platinum-based oxygen reduction electrocatalysts. *Acc. Chem. Res.* **46**, 1848–1857 (2013).
4. Y. J. Wang, N. Zhao, B. Fang, H. Li, X. T. Bi, H. Wang, Carbon-supported Pt-based alloy electrocatalysts for the oxygen reduction reaction in polymer electrolyte membrane fuel cells: particle size, shape, and composition manipulation and their impact to activity. *Chem. Rev.* **115**, 3433–3467 (2015).
5. Z. Peng, H. Yang, Designer platinum nanoparticles: control of shape, composition in alloy, nanostructure and electrocatalytic property. *Nano Today* **4**, 143–164 (2009).
6. D. Wang, H. L. Xin, R. Hovden, H. Wang, Y. Yu, D. A. Muller, F. J. DiSalvo, H. D. Abruña, Structurally ordered intermetallic platinum-cobalt core-shell nanoparticles with enhanced activity and stability as oxygen reduction electrocatalysts. *Nat. Mater.* **12**, 81–87 (2013).
7. C. Wang, M. Chi, G. Wang, D. van der Vliet, D. Li, K. More, H. Wang, J. A. Schlueter, N. M. Markovic, V. R. Stamenkovic, Correlation between surface chemistry and electrocatalytic properties of monodisperse Pt<sub>x</sub>Ni<sub>1-x</sub> nanoparticles. *Adv. Funct. Mater.* **21**, 147–152 (2011).
8. D. F. van der Vliet, C. Wang, D. Tripkovic, D. Strmcnik, X. F. Zhang, M. K. Debe, R. T. Atanasoski, N. M. Markovic, V. R. Stamenkovic, Mesostructured thin films as electrocatalysts with tunable composition and surface morphology. *Nat. Mater.* **11**, 1051–1058 (2012).
9. V. R. Stamenkovic, B. S. Mun, M. Arenz, K. J. J. Mayrhofer, C. A. Lucas, G. Wang, P. N. Ross, N. M. Markovic. Trends in electrocatalysis on extended and nanoscale Pt-bimetallic alloy surface. *Nat. Mater.* **6**, 241–247 (2007).
10. D. F. van der Vliet, C. Wang, D. Li, A. P. Paulikas, J. Greeley, R. B. Rankin, D. Strmcnik, D. Tripkovic, N. M. Markovic, V. R. Stamenkovic, Unique electrochemical adsorption properties of Pt-skin surfaces. *Angew. Chem. Int. Ed.* **51**, 3139–3142 (2012).
11. C. Cui, L. Gan, M. Heggen, S. Rudi, P. Strasser, Compositional segregation in shaped Pt alloy nanoparticles and their structural behavior during electrocatalysis. *Nat. Mater.* **12**, 765–771 (2013).
12. V. R. Stamenkovic, B. S. Mun, K. J. J. Mayrhofer, P. N. Ross, N. M. Marković, Effect of Surface Composition on Electronic Structure, Stability, and Electrocatalytic Properties of Pt-Transition Metal Alloys: Pt-Skin versus Pt-Skeleton Surfaces. *J. Am. Chem. Soc.* **128**, 8813–8819 (2006).

13. F. Calle-Vallejo, J. I. Martínez, J. M. García, Lastra, P. Sautet, D. Loffreda, Fast prediction of adsorption properties for platinum nanocatalysts with generalized coordination numbers. *Angew. Chem. Int. Ed.* **53**, 8316–8319 (2014).
14. F. Calle-Vallejo, J. Tymoczko, V. Colic, Q. H. Vu, M. D. Pohl, K. Morgenstern, D. Loffreda, P. Sautet, W. Schuhmann, A. S. Bandarenka, Finding optimal surface sites on heterogeneous catalysts by counting nearest neighbors. *Science* **350**, 185–189 (2015).
15. M. E. Escribano, P. Malacrida, M. H. Hansen, U. G. V. Hansen, A. V. Palenzuela, V. Tripkovic, J. Schiøtz, J. Rossmeisl, I. E. L. Stephens, I. Chorkendorff, Tuning the activity of Pt alloy electrocatalysts by means of the lanthanide contraction. *Science* **352**, 73–76 (2016).
16. A. Fortunelli, W. A. Gorddard III, L. Sementa, G. Barcaro, F. R. Negreiros, A. J. Botero, The atomistic origin of the extraordinary oxygen reduction activity of Pt<sub>3</sub>Ni<sub>7</sub> fuel cell catalysts. *Chem. Sci.* **6**, 3915–3925 (2015).
17. S. Choi, S. Xie, M. Shao, J. H. Odell, N. Lu, H. C. Peng, L. Protsailo, S. Guerrero, J. Park, X. Xia, J. Wang, M. J. Kim, Y. Xia, Synthesis and characterization of 9 nm Pt-Ni octahedral with a record high activity of 3.3A/mg<sub>Pt</sub> for the oxygen reduction reaction. *Nano Lett.* **13**, 3420–3425 (2013).
18. X. Huang, Z. Zhao, Y. Chen, E. Zhu, M. Li, X. Duan, Y. Huang, A rational design of carbon-supported dispersive Pt-based octahedral as efficient oxygen reduction reaction catalysts. *Energy Environ Sci.* **7**, 2957–2962 (2014).
19. X. Huang, Z. Zhao, L. Cao, Y. Chen, E. Zhu, Z. Lin, M. Li, A. Yan, A. Zettl, Y. M. Wang, X. Duan, T. Mueller, Y. Huang, High-performance transition metal-doped Pt<sub>3</sub>Ni octahedral for oxygen reduction reaction. *Science* **348**, 1230–1234 (2015).
20. H. Zhu, S. Zhang, S. Guo, D. Su, S. Sun, Synthetic control of FePtM nanorods (M = Cu, Ni) to enhance the oxygen reduction reaction. *J. Am. Chem. Soc.* **135**, 7130–7133 (2013).
21. S. Guo, D. Li, H. Zhu, S. Zhang, N. M. Markovic, V. R. Stamenkovic, S. Sun, FePt and CoPt nanowires as efficient catalysts for the oxygen reduction reaction. *Angew. Chem. Int. Ed.* **52**, 3465–3468 (2013).
22. L. Zhang, L. T. Roling, X. Wang, M. Vara, M. Chi, J. Liu, S. Choi, J. Park, J. A. Herron, Z. Xie, M. Mavrikakis, Y. Xia, Platinum-based nanocages with subnanometer-thick walls and well-defined, controllable facets. *Science* **24**, 412–416 (2015).
23. C. Chen, Y. Kang, Z. Huo, Z. Zhu, W. Huang, H. L. Xin, J. D. Snyder, D. Li, J. A. Herron, M. Mavrikakis, M. Chi, K. L. More, Y. Li, N. M. Markovic, G. A. Somorjai, P. Yang, V. R. Stamenkovic, Highly crystalline multimetallic nanoframes with three-dimensional electrocatalytic surface. *Science* **343**, 1339–1343 (2014).
24. S. Zhang, Y. Hao, D. Su, V. V. T. Doan-Nguyen, Y. Wu, J. Li, S. Sun, C. B. Murray, Monodisperse core/Shell Ni/FePt nanoparticles and their conversion to Ni/Pt to catalyze oxygen reduction, *J. Am. Chem. Soc.* **136**, 15921–15924, (2014).
25. Materials and methods are available as supplementary materials
26. L. Tang, B. Han, K. Persson, C. Friesen, T. He, K. Sieradzki, G. Ceder, Electrochemical stability of nanometer-scale Pt particles in acidic environments, *J. Am. Chem. Soc.* **132**, 596–600, (2010).

27. L. Tang, X. Li, R. C. Cammarata, C. Friesen, K. Sieradzki, Electrochemical stability of elemental metal nanoparticles, *J. Am. Chem. Soc.* **132**, 11722-11726, (2010).
28. C. F. Sanz-Navarro, P. O. Astrand, D. Chen, M. Ronning, A. C. T. van Duin, T. Jacob and W. A. Goddard III, Molecular Dynamics Simulations of the Interactions between Platinum Clusters and Carbon Platelets, *J. Phys. Chem. A*, **112**, 1392 – 1402 (2008).
29. F. Cleri, V. Rosato, Tight-binding potentials for transition metals and alloys, *Phys. Rev. B*. **48**, 22-33, (1993).
30. Y. Sha, T. H. Yu, B. V. Merinov, P. Shirvastian, W. A. Goddard III, Oxygen hydration mechanism for the oxygen reduction reaction at Pt and Pd fuel cell catalysts. *J. Phys. Chem. Lett.* **2**, 572–576 (2011).
31. D. Faken, H. Jonsson, Systematic analysis of local atomic structure combined with 3D computer graphics. *Comput. Mater. Sci.* **2**, 279–286 (1994).
32. S. Schnur, A. Groß, Strain and coordination effects in the adsorption properties of early transition metals: A density-functional theory study, *Phys. Rev. B*. **81**,033402 (2010).
33. J. D. Honeycutt, H. C. Andersen. Molecular dynamics study of melting and freezing of small Lennard-Jones clusters. *J. Phys. Chem.* **91**, 4950-4963 (1987).
34. A. Stukowski, Structure identification methods for atomistic simulations of crystalline materials. *Model. Simul. Mater. Sci. Eng.* **20**, 045021 (2012).
35. M. F. Francis, & W. A. Curtin, Mechanical work makes important contributions to surface chemistry at steps. *Nat. Commun.* **6**, 6261 (2015).
36. S. Zhang, X. Zhang, G. Jiang, H. Zhu, S. Guo, D. Su, G. Lu, S. Sun, Tuning Nanoparticle Structure and Surface Strain for Catalysis Optimization, *J. Am. Chem. Soc.* **136**, 7734–7739, (2014).
37. B. Ravel, M. Newville, ATHENA, ARTEMIS, HEPHAESTUS: data analysis for X-ray absorption spectroscopy using IFEFFIT. *J. of synchrotron radiat.* **12**, 537-541 (2005).
38. A. Ankudinov, B. Ravel, J. Rehr, S. Conradson, Real-space multiple-scattering calculation and interpretation of x-ray-absorption near-edge structure. *Phys. Rev. B*, **58**, 7565-7576 (1998).

## ACKNOWLEDGEMENTS

The Advanced Light Source is supported by the Director, Office of Science, Office of Basic Energy Sciences, of the U.S. Department of Energy under Contract No. DE-AC02-05CH11231. We thank Dr. Matthew A. Marcus at ALS for the support during the acquisition of XAS data, and C. Wu for help on EXAFS data analysis. R.Y. acknowledges support from the National Natural Science Foundation of China project number 51525102, 51390475, 51371102. The aberration-corrected transmission electron microscopy results were achieved (in part) using Titan 80-300 and JEM-ARM 200F. In this work we used the resources of the National Center for Electron Microscopy in Beijing. A patent application on this subject has been filed. WAG, AF, BM, and TC acknowledge support from NSF (CBET-1512759)

## SUPPLEMENTARY MATERIALS

Materials and Methods

Figs. S1 to S13

Tables S1 to S2

References (16, 37-38)

# Ultrafine Jagged Platinum Nanowires Enable Record-High Platinum Mass Activity for Oxygen Reduction Reaction

Mufan Li<sup>1</sup>, Zipeng Zhao<sup>2</sup>, Tao Cheng<sup>3</sup>, Alessandro Fortunelli<sup>3,4</sup>, Chih-Yen Chen<sup>2</sup>, Rong Yu<sup>5</sup>, Qinghua Zhang<sup>6</sup>, Lin Gu<sup>6</sup>, Boris Merinov<sup>3</sup>, Zhaoyang Lin<sup>1</sup>, Enbo Zhu<sup>2</sup>, Qinghua Zhang<sup>6</sup>, Ted Yu<sup>3,7</sup>, Qingying Jia<sup>8</sup>, Jinghua Guo<sup>9</sup>, Liang Zhang<sup>9</sup>, William A. Goddard III<sup>3\*</sup>, Yu Huang<sup>2,10\*</sup> and Xiangfeng Duan<sup>1,10\*</sup>

<sup>1</sup>Department of Chemistry and Biochemistry, University of California, Los Angeles, California 90095, United States

<sup>2</sup>Department of Materials Science and Engineering, University of California, Los Angeles, California 90095, United States

<sup>3</sup>Materials and Process Simulation Center, California Institute of Technology, Pasadena, California 91125, United States

<sup>4</sup>CNR-ICCOM, Consiglio Nazionale delle Ricerche, 56124, Pisa, Italy

<sup>5</sup>National Center for Electron Microscopy in Beijing, School of Materials Science and Engineering, Tsinghua University, Beijing 100084, P. R. China

<sup>6</sup>Institute of Physics, Chinese Academy of Sciences, Beijing 100190, P. R. China

<sup>7</sup>Department of Chemical Engineering, California State University, Long Beach, California 90840, United States

<sup>8</sup>Department of Chemistry and Chemical Biology, Northeastern University, Boston, Massachusetts 02115, United States

<sup>9</sup>Materials Sciences Division, Lawrence Berkeley National Laboratory, Berkeley, California 94720, United States

<sup>10</sup>California NanoSystems Institute, University of California, Los Angeles, California 90095, United States

\*Correspondence author. Email: wag@wag.caltech.edu (W.G.); yhuang@seas.ucla.edu (Y.H.); xduan@chem.ucla.edu (X.D.)

## Supplementary Materials:

### Materials and Methods

#### 1. Chemicals:

Platinum(II) acetylacetonate (Pt(acac)<sub>2</sub>, 97%), nickel(II) acetylacetonate (Ni(acac)<sub>2</sub>, 95%), cobalt (II) acetylacetonate (Co(acac)<sub>2</sub>, 97%), glucose, tungsten(0) hexacarbonyl (W(CO)<sub>6</sub>, 97%), Polyvinylpyrrolidone (PVP mw. 40,000), Oleylamine (> 70%), 1-octadecene (ODE, > 90%),

Ethanol (200 proof), perchloric acid ( $\text{HClO}_4$ , 70%, PPT Grade) were all purchased from Sigma-Aldrich. All aqueous solutions were prepared using deionized (DI) water (18.2 M $\Omega$ /cm) obtained from an ultra-pure purification system (Aqua Solutions).

## 2. Preparation of jagged Pt nanowire (J-PtNW) catalysts

In a typical synthesis, 0.025 mmol  $\text{Pt}(\text{acac})_2$ , 0.10 mmol  $\text{Ni}(\text{acac})_2$  and 0.75 mmol glucose were pre-dissolved in mixture of 2 mL 1-octadecene (ODE) and 3 mL oleylamine (OAm). After sonicated for 10 min, 0.0015 mmol PVP (mw. 40,000) and 0.0050 mmol  $\text{W}(\text{CO})_6$  were added into the pre-dispersed solution and sealed with argon. The mixture was further heated up to 140 °C for 6 hours to obtain Pt/NiO core/shell nanowires, which were then washed and cleaned using acetone/cyclohexane/ethanol mixture, and collected by centrifuging at 7000 rpm.

The as-prepared Pt/NiO NWs were suspended in 15 mL cyclohexane/ethanol mixture. To load the sample on to carbon black, 36 mg of carbon black was added for each 4 mg Pt/NiO NWs and sonicated for 2 hours. The resulting Pt/NiO-NWs/C catalysts were collected by centrifugation and cleaned with cyclohexane/ethanol mixture, placed in an alumina boat and annealed at 450 °C in Ar/H<sub>2</sub>: 97/3 with 100 sccm flow rate in a home-build tube furnace.

## 3. Preparation of regular Pt nanowire (R-PtNW) catalysts

In a typical synthesis, 0.025 mmol platinum  $\text{Pt}(\text{acac})_2$ , 0.10 mmol  $\text{Co}(\text{acac})_2$  and 0.75 mmol glucose were pre-dissolved in mixture of 2 mL 1-octadecene (ODE) and 3 mL oleylamine (OAm). After sonicated for 10 min, 0.0015 mmol PVP (mw. 40,000) and 0.0050 mmol  $\text{W}(\text{CO})_6$  were added into the pre-dispersed solution and sealed with argon. The mixture was further heated up to 120 °C for 3 hours to get regular nanowires. After cleaned the product by acetone/cyclohexane/ethanol mixture, the R-PtNWs were collected by centrifuging at 7000 rpm, and re-suspended in 15 mL cyclohexane/ethanol mixture and loaded onto carbon black using the same approach described above, flowed by a moderate annealing at 250 °C.

## 4. Preparation of Pt-Ni nanoparticles

In a typical synthesis, 0.025 mmol platinum  $\text{Pt}(\text{acac})_2$ , 0.075 mmol  $\text{Ni}(\text{acac})_2$  and 0.75 mmol glucose were pre-dissolved in mixture of 2 mL 1-octadecene (ODE) and 3 mL oleylamine (OAm). After sonication for 10 min, 0.0015 mmol PVP (mw. 40,000) and 0.050 mmol  $\text{W}(\text{CO})_6$  were added into the pre-dispersed solution and sealed with argon. The mixture was further heated up to 170 °C for 6 hours with stirring to obtain PtNi nanoparticles (NPs). After cleaning with a mixture of acetone/cyclohexane/ethanol, the PtNi NPs were collected by centrifuging at 12,000 rpm, and re-suspended in 15 mL cyclohexane/ethanol mixture and loaded onto carbon black using the same approach described above, flowed by a thermal annealing at 450 °C.

## 5. Preparation of Pt-Co nanowires

In a typical synthesis, 0.025 mmol platinum  $\text{Pt}(\text{acac})_2$ , 0.100 mmol  $\text{Ni}(\text{acac})_2$  and 0.75 mmol glucose were pre-dissolved in mixture of 2 mL 1-octadecene (ODE) and 3 mL oleylamine (OAm). After sonication for 10 min, 0.0015 mmol PVP (mw. 40,000) and 0.0050 mmol  $\text{W}(\text{CO})_6$  were added into the pre-dispersed solution and sealed with argon. The mixture was further heated up to 170 °C for 6 hours with stirring to obtain Pt/Co core/shell nanowires (NWs). After cleaning with a mixture of acetone/cyclohexane/ethanol, the PtNi NPs were collected by centrifuging at 12,000 rpm, and re-suspended in 15 mL cyclohexane/ethanol mixture and loaded onto carbon black using the same approach described above, flowed by a thermal annealing at 450 °C.

## 6. Structure and composition characterization

Scanning electron microscope (SEM) and Energy-dispersive X-ray spectroscopy (EDS) were collected on ZEISS Supra 40VP SEM. The EDS analysis of the as-prepared Pt/NiO core/shell NWs show a Pt/Ni ratio of 15/85 (Fig. S3A, B).

Powder X-ray diffraction (XRD) patterns were collected on a Panalytical X'Pert Pro X-ray Powder Diffractometer with Cu-K $\alpha$  radiation.

X-ray photoelectron spectroscopy (XPS) tests were done with Kratos AXIS Ultra DLD spectrometer. Transmission electron microscopy (TEM) images were carried out on an FEI T12 transmission electron microscope operated at 120 kV. High resolution TEM images (HRTEM), energy-dispersive X-ray spectroscopy (EDS) line-scan file were taken on FEI TITAN transmission electron microscope operated at 300 kV. The high-angle annular dark-field scanning transmission electron microscope (HAADF-STEM) were performed on aberration corrected TEM. The samples were prepared by dropping ethanol dispersion of catalysts onto carbon-coated molybdenum TEM grids.

The concentration of catalysts was determined by the inductively coupled plasma (ICP) atomic emission spectroscopy. The ICP sample we used for jagged Pt nanowires was annealed material before electro chemical activation. The Pt loading for J-PtNWs was 2.2  $\mu\text{g}/\text{cm}^2$  on glassy carbon electrode. ICP test of the concentrated electrolyte from 10 activation processes indicates 1.2% Pt is leached off from the PtNi NWs during the dealloying process, suggesting >98.8% of Pt was retained during the electrochemical activation process.

## 7. Electrochemical experiment

All the electrochemical experiments were conducted using a three-electrode cell system. The working electrode was a glassy carbon rotating disk electrode (RDE) from Pine Instruments, the glassy carbon geometry area is 0.196  $\text{cm}^2$ . Pt wire and Ag/AgCl (1 M Cl<sup>-</sup>) were used as the counter and reference electrodes respectively. Pt loadings were 2.2  $\mu\text{g}/\text{cm}^2$ , 2.55  $\mu\text{g}/\text{cm}^2$ , and 7.65  $\mu\text{g}/\text{cm}^2$  for J-Pt NWs, R-Pt NWs, and Pt/C respectively (All the loading mass were normalized over the geometric electrode area of 0.196  $\text{cm}^2$ ).

Cyclic voltammetry (CV) activations were performed in N<sub>2</sub>-saturated 0.1 M HClO<sub>4</sub> electrolyte with potential scan rate of 100 mVs<sup>-1</sup>. All the electrochemical active surface area (ECSA) was determined by integrating hydrogen adsorption charge on CV curve by assuming a value of 210  $\mu\text{C}/\text{cm}^2$  for the adsorption of a hydrogen monolayer. Double-layer correction was applied. The ECSA for J-PtNWs, R-PtNWs, and Pt/C were calculated via same method.

Oxygen reduction reaction (ORR) tests were conducted in N<sub>2</sub>-saturated 0.1 M HClO<sub>4</sub> electrolyte with potential scan rate of 20 mVs<sup>-1</sup>. The current density of ORR polarize curve were iR corrected during the measurements.

The stability test was performed at room temperature in O<sub>2</sub>-saturated 0.1 M HClO<sub>4</sub> solution with a potential scan rate of 100 mVs<sup>-1</sup>.

For CV test in alkaline solution, the J-PtNWs and partially activated (150 cycles) Pt-Ni alloy nanowires were firstly activated in N<sub>2</sub>-saturated 0.1 M HClO<sub>4</sub> electrolyte with potential scan rate of 100 mVs<sup>-1</sup>. After rinsed the electrode by DI water, the CV was performed in N<sub>2</sub>-saturated 0.1 M KOH electrolyte at a scan rate of 50 mVs<sup>-1</sup>.

## 8. Computational studies

To generate realistic structural models of PtNi alloy nanowires, we extended the computational protocol developed previously to simulate Ni de-alloying of Pt<sub>3</sub>Ni<sub>7</sub> nanoparticles (0D systems) (16).

Thus:

1. We started from an infinite nanowire (1D system), based on the *fcc* Pt crystal structure. The *z* axis of the nanowire is along the (111) crystal direction, while in the *xy* plane we have 13 Pt atoms along the *x* axis and 9 Pt atoms are along the *y* axis. This choice was made to expose some (100) facets along the NW axis
2. We built a periodic model by replicating 220 individual unit cells along the axis of the wire
3. The overall ratio of Ni to Pt is 85: 15 consistent with experiment, which was achieved by randomly replacing 85% of the Pt atoms with Ni atoms, while ensuring that the Ni composition is roughly constant along the nanowire axis.
4. We erase all the Ni atoms and perform a fixed-cell conjugate-gradient local relaxation using the ReaxFF force field. Here at each conjugate-gradient step limits the maximum change in Cartesian coordinates to 0.1 Å to ensure a smooth local minimization that avoids disruption of the original random *fcc* framework. The convergence threshold criteria are  $4 \times 10^{-6}$  eV on the energy and  $4 \times 10^{-8}$  eV/Å on the gradient.
5. We perform a second local relaxation allowing the cell dimension in the *z*-direction to equilibrate at a pressure of 1 atm.
6. We perform a final NPT Molecular Dynamics (MD) simulation at 343 K for 520 ps (20 ps equilibration followed by a 500 ps run)
7. We delete the least coordinated atoms which would be further leached away during ORR cycling and perform an additional NPT Molecular Dynamics (MD) simulation at 343 K for 520 ps (20 ps equilibration followed by a 500 ps run)
8. We locally relax the final structure using a SMA force field.

This protocol, in which we simultaneously remove Ni throughout the initial *fcc* nanostructure and locally relax and equilibrate the resulting configuration, is intended as a simplified mimic of the complex kinetics-driven de-alloying process induced by during electrochemical activation, where Ni surface atoms are progressively leached out of the system. The ReaxFF reactive force could be used in a more realistic gradual depletion of the Ni atoms under realistic conditions, but the size of the system and the long time scales of ORR-induced de-alloying makes this more realistic simulation impractical. However, we consider that the smooth local minimization of the initial randomly sparse *fcc* framework of Pt atoms provides a reasonable approximation to the relaxation processes through metastable configurations that retain memory of the original pattern. Our assumption that all Ni atoms are removed in step (4), corresponds in our previous nanoparticle study to propagating the topmost 4/6 surface layers devoid of Ni into the bulk (16). We consider that the experimental evidence showing that all Ni atoms are leached out in these small diameter nanowires fully justifies this approach. It can be noted that the ReaxFF reactive force field (28) has been derived from extensive quantum mechanics calculations validated by comparing to experiment and is used in the process generating structure and overall morphology of dealloyed NWs in which directionality terms in

the potential are important. However, this force field tends to overestimate surface distances so that the SMA potential (29) was finally used to compare with experimental data from extended x-ray absorption fine structure (EXAFS) analysis.

We compare the nanowire structural characteristics with those of the Pt<sub>3</sub>Ni<sub>7</sub> nanoporous particle obtained by de-alloying a 10-nm-diameter *fcc* Pt<sub>3</sub>Ni<sub>7</sub> nanoparticle as a representative nanoparticles exhibiting peak ORR performance.

Thus we use:

1. Radial distribution functions (RDF);
2. A coordination vector threshold to distinguish surface and bulk atoms;
3. Number of first neighbors (coordination number);
4. Atomic stress and 5-fold index;
5. Analysis of surface arrangement in terms of rhombic structures.

The coordination vector is defined as the sum of all the vectors pointing from first-neighbors to the given atom, and a given Pt atom is defined as a bulk atom if the norm of the coordination vector is smaller than a given threshold (0.6 Å), and as a surface atom otherwise, in analogy with the approach taken in Ref. (16). The Cauchy atomic stress tensors on atom *i* ( $\sigma^i$ ) used in Fig.3 is defined as [V. Vitek, T. Egami, Atomic Level Stresses in Solids and Liquids. *Physica Status Solidi (b)* **144**, 145-156 (1987)]:

$$\sigma^i = \frac{1}{\Omega_i} \cdot \left\{ \frac{1}{2} \sum_j \mathbf{F}_{ij} \otimes \mathbf{r}_{ij} \right\}$$

where  $\Omega_i$  is the atomic volume of atom *i*, and the sum is taken over all *j*-neighbors of *i*, at a distance  $\mathbf{r}_{ij}$  each and exerting a force  $\mathbf{F}_{ij}$  upon *i*. Given that atomic volumes are not well defined for a deformed solid, we follow common practice of reporting in Fig.3 the products  $\sigma^i \cdot \Omega_i$  in units of atm · nm<sup>3</sup>. Another useful quantity reported in the main text is the surface energy ( $E_{\text{surface}}$ ), defined as:

$$E_{\text{surface}} = \frac{1}{A} \cdot \{ E_{\text{system}} - N E_{\text{bulk}} \}$$

where A is the surface area, which is the excess energy of the system ( $E_{\text{system}}$ ) with respect to the bulk ( $E_{\text{bulk}}$ ). The 5-fold index is finally defined as the ratio of icosahedral fingerprint [5,5,5] triplets to the total number of triplets in Common Neighbor Analysis (31-34).

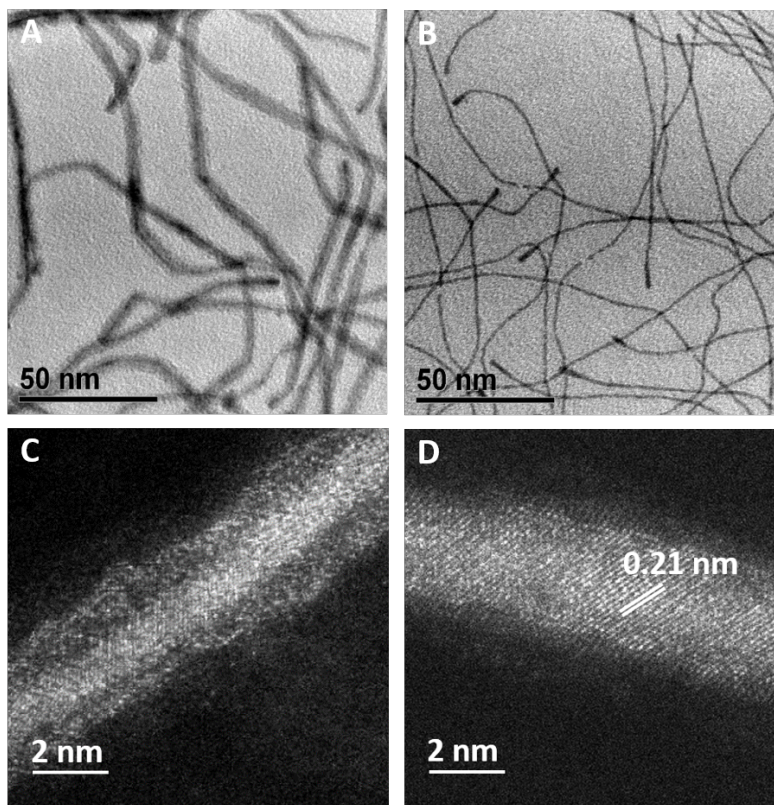
As shown in Figs. 3, S11 and Table S2, the jagged Pt nanowire exhibits structural features that are qualitatively and quantitatively similar to de-alloyed Pt<sub>3</sub>Ni<sub>7</sub> nanoparticles (16), but with an increase in ORR-favorable patterns, thus explaining our experimentally observed superior ORR catalytic activity for these NW. A configuration from the protocol using Reactive Molecular Dynamics (steps 1-7 above) together with the structure locally relaxed using SMA potential are provided as a further Supplementary Material.

## 9. XAS data collection and analysis.

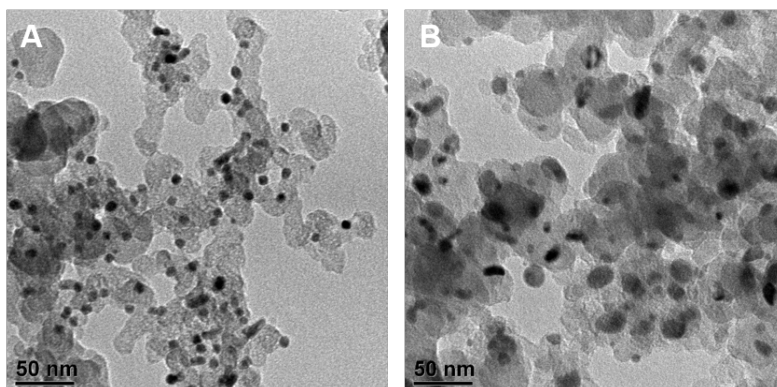
The J-PtNWs/C powders were collected via sonication from RDE after CV activation and ORR test. The sample for XAS study was washed and dispersed in ethanol. The Pt loading is 3.6% based on ICP result. X-ray absorption spectroscopy (XAS) experiments were performed at Advanced Light Source (beamline 10.3.2) in Lawrence Berkeley National Laboratory. Full range Pt L<sub>3</sub> spectra were collected in the fluorescence mode at room temperature with a Pt reference

foil positioned between I2 and I3 as a reference. The data were processed and fitted using the Iffeffit-based Athena and Artemis programs (37). Scans were calibrated, aligned and normalized with background removed using the IFEFFIT suite (37). The  $\chi(R)$  were modeled using single scattering paths calculated by FEFF6 (38). The extended x-ray absorption fine structure (EXAFS) spectrum was fitted using a *fcc* platinum model. The Pt L<sub>3</sub>-edge XANES region is shown in Fig. S10.

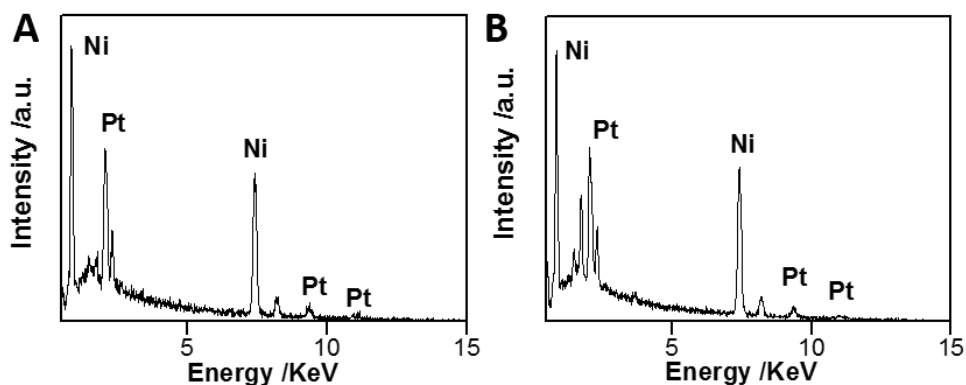
### Supplementary Figures



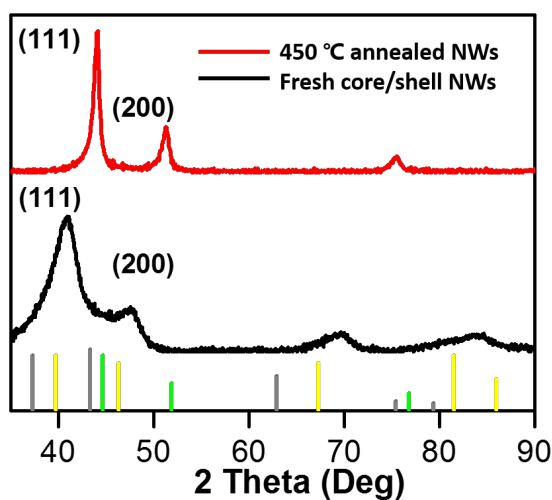
**Fig. S1.** (A and B) TEM images for Pt/NiO core/shell nanowires and regular nanowires. (C and D) STEM images for Pt/NiO nanowires/C before and after annealing at 450 °C in Ar/H<sub>2</sub> (97/3) atmosphere for 12 hours.



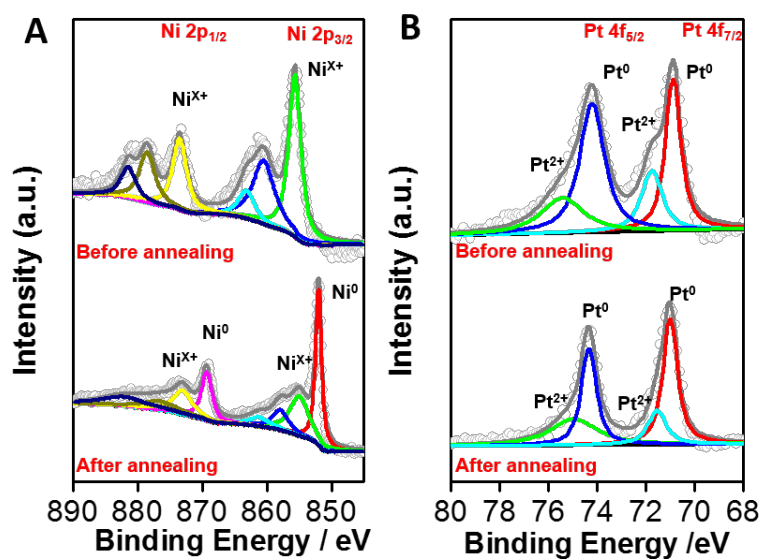
**Fig. S2.** TEM images of PtNi NPs (A) before and (B) after annealing at 450 °C in Ar/H<sub>2</sub> (97/3) atmosphere for 12 hours.



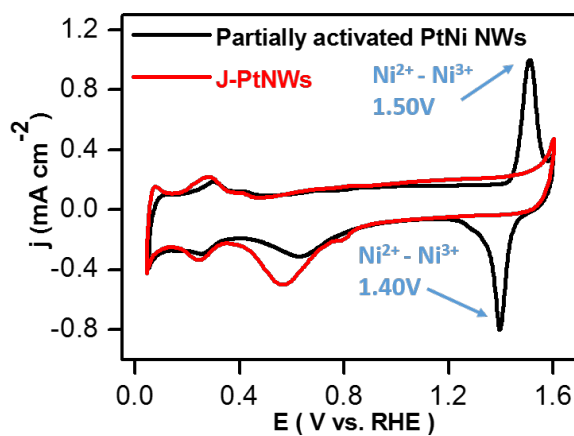
**Fig. S3.** (A) EDS spectrum of the as-prepared Pt/NiO core/shell NWs. (B) EDS spectrum the Pt-Ni alloy NWs obtained after 450 °C annealing.



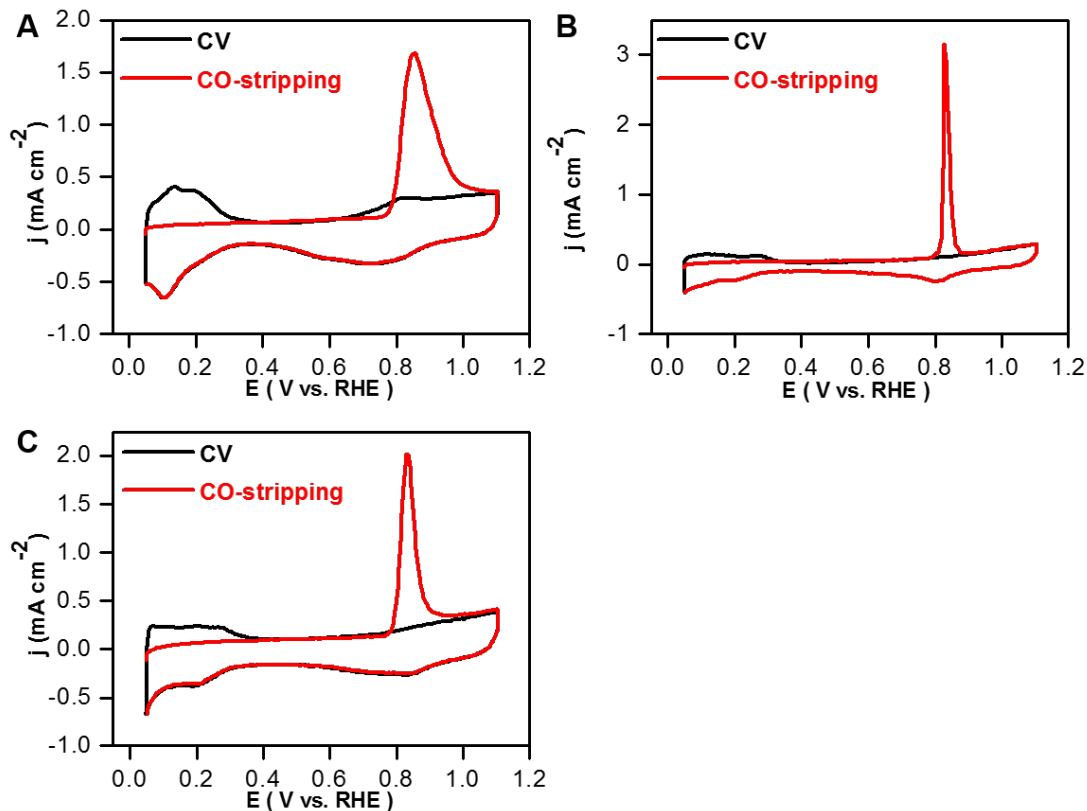
**Fig. S4.** XRD spectra comparison of fresh and 450 °C annealed and fresh Pt/NiO core/shell nanowires/C. The standard XRD pattern for *fcc* NiO, Pt, Ni are displayed as grey, yellow, and green bars. The crystallinity of fresh sample (black line) showed existence of non-*fcc* phase, and since the size of Pt core NWs is ultrafine (sub 2 nm), the result XRD peak for fresh sample is broadened. The overlapped (111) and (200) peak region could be caused by the existence of NiO. For 450 °C annealed sample (red line), the narrowed symmetric XRD peak suggested the formation of larger alloyed crystal. The result (111) peak ( $2\theta = 44.0^\circ$ ) was relatively closer to Ni (111) ( $2\theta = 44.6^\circ$ ) than that of Pt (111) ( $2\theta = 39.7^\circ$ ), indicates the result alloy is Ni-rich which is constant with our EDS result (Fig. S3B).



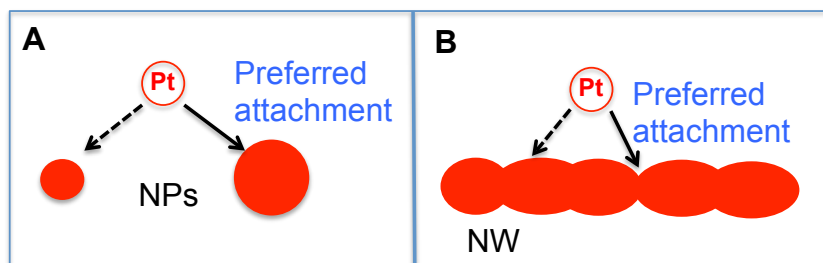
**Fig. S5.** (A) Ni, (B) Pt XPS spectra comparison before and after annealing of Pt/NiO core/shell nanowires/C.



**Fig. S6.** The cyclic voltammometry (CV) curves for partially activated Pt-Ni alloy NWs (150 cycles in 0.1 M HClO<sub>4</sub> solution) and J-PtNWs in alkaline electrolyte with scan rate of 50 mVs<sup>-1</sup>. The current densities were normalized to the geometric area of the RDE (0.196 cm<sup>2</sup>).

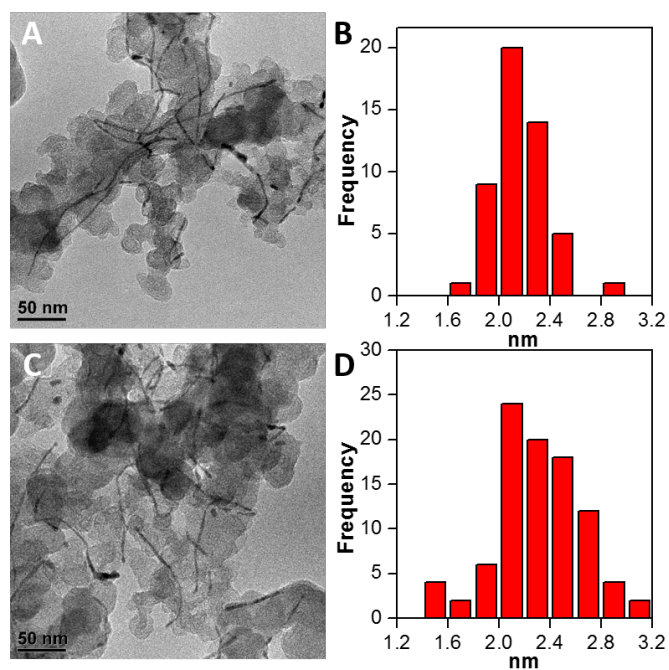


**Fig. S7.** The CV and CO-stripping curves of the (A) Pt/C, (B) R-PtNWs, and (C) J-PtNWs. All the CO-stripping curves were recorded at room temperature in CO-saturated 0.1 M HClO<sub>4</sub> solution at scan rate of 50 mVs<sup>-1</sup>. The current densities were normalized to the geometric area of the RDE (0.196 cm<sup>2</sup>). The ECSA<sub>Hupd</sub>: ECSA<sub>CO</sub> ratio is 1:1.03, 1:1.06, 1:1.05 for Pt/C, R-PtNWs, J-PtNWs respectively.

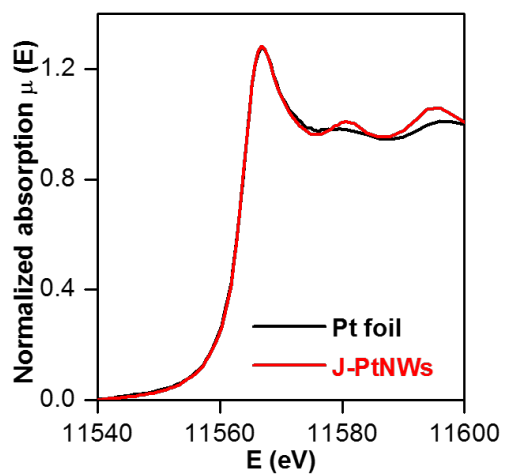


**Fig. S8.** Ostwald ripening, in which Pt atoms are dissolved from one nanostructure and reattach to another one, can often lead to aggregation of ultrafine nanostructures. In such processes, the dissolved Pt atoms tend to reattach at new locations that are more energetically favorable, such as locations with smaller curvature or more coordinated neighbors. In this scenario the energetically more favorable sites for NPs are likely NPs with larger size because of smaller curvature (larger radius of curvature) (A), leading to Ostwald ripening and serious loss of ECSA. However, for 1D NWs, the energetically favorable sites are more likely located at the narrower constriction region with negative curvature (B), which would promote atom attachment to the

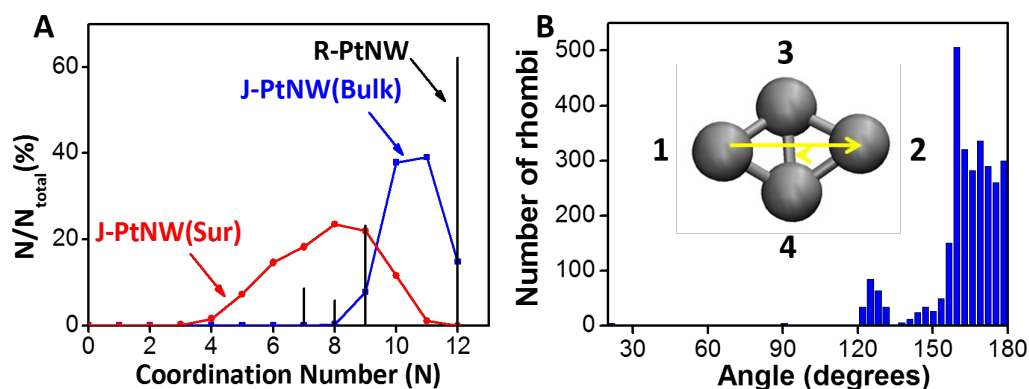
narrow regions and prevent the breakup of 1D structure and thus lead to further stabilization of 1D NW structure.



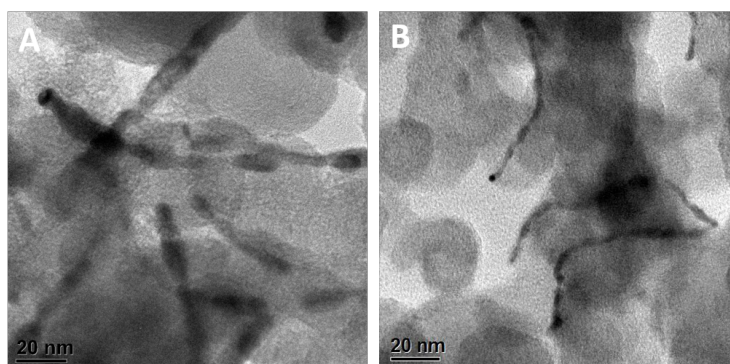
**Fig. S9.** (A), (C) TEM images, and (C), (D) NWs diameter distribution chart for jagged PtNWs after CV activation and ADT test respectively.



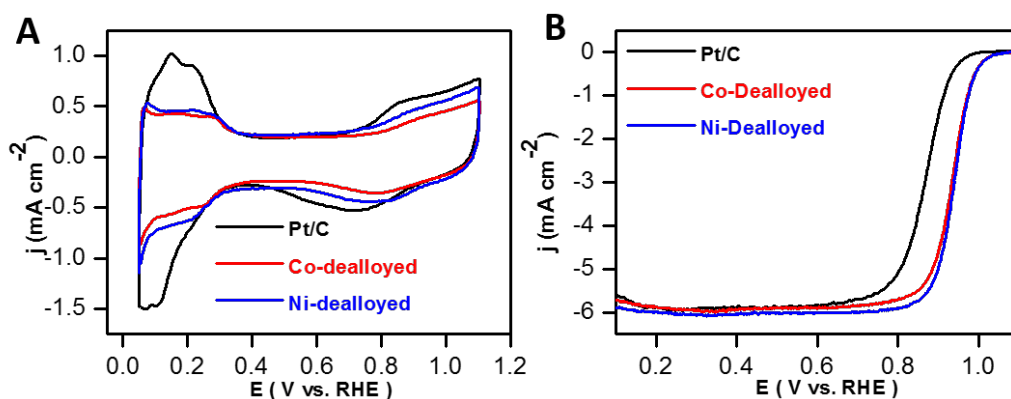
**Fig. S10.** Pt L<sub>3</sub>-edge XANES of J-PtNWs after electrochemical test compared to Pt foil Standard.



**Fig. S11.** (A) Coordination number for surface atoms (red) and bulk atoms (blue) of the J-PtNWs, and atoms (black) of R-PtNWs evaluated by counting all neighbors within a distance cut-off of 3.0 Å. (B) Schematic depiction of a rhombus (inset) and the distribution of the dihedral angle between the two triangles of the rhombus as defined by the angle formed between the two lines connecting atom 1 and 2 to the middle point of atom 3,4 respectively (highlighted by the yellow arrows in the inset). Most of the angles are between 156° and 180°, which suggest that the surface of the J-PtNWs are highly comparable typical crystalline structure.



**Fig. S12.** (A) Annealed PtCo NWs/C samples (B) De-alloyed PtCo NWs/C. The de-alloy process was conducted in N<sub>2</sub>-saturated 0.1M HClO<sub>4</sub> with a scan rate of 100 mV/s



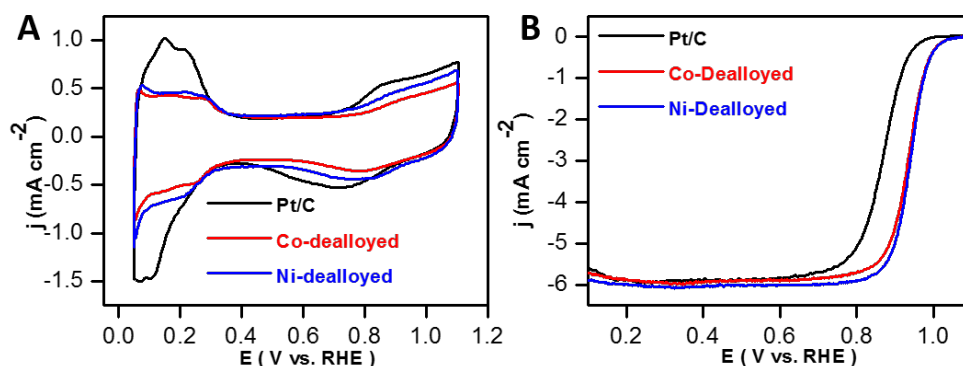


**Fig. S13.** (A) CV and (B) ORR polarization curves for the Pt/C, Co-dealloyed, and Ni-dealloyed J-PtNWs, respectively.

**Table S1.** EXAFS results obtained by fitting the Pt  $L_3$  edge data for the J-PtNWs.  $S_0^2$  is fixed at 0.83 for Pt as obtained by fitting the reference foils. The fit was done in  $R$ -space,  $k^{1,2,3}$  weighting with  $1.50 < R < 3.11$  Å and  $\Delta k = 3.06 - 13.39$  Å $^{-1}$  used. R-factor is a measure of the goodness of fit. The statistical errors of the least-squares fit were determined by ARTEMIS

Path	R (Å)	N	$E_0$ (eV)	$\sigma^2$ (Å $^2$ )	R-factor
Pt-Pt	2.71±0.01	9.1±1.0	6.8±0.6	0.007±0.003	0.007

**Table S2.** Geometric analysis of the final predicted structure of 46-nm-long de-alloyed Pt nanowire (snapshot from the RMD trajectory) compared with the typical predicted structure of a fully de-alloyed Pt $_3$ Ni $_7$  NP (initially 10 nm in diameter, finally around 8 nm in diameter) taken from (16).

	vdW Surface Area (m $^2$ /g $_{Pt}$ )	Surface Atoms N (%)	ORR-favorable Rhombi N (%)
De-alloyed NW	110	49%	76 %
NP (70% Ni)	61	26%	57 %